iScience

Article

A cobalt-aluminium layered double hydroxide with a nickel core-shell structure nanocomposite for supercapacitor applications

Graphical abstract

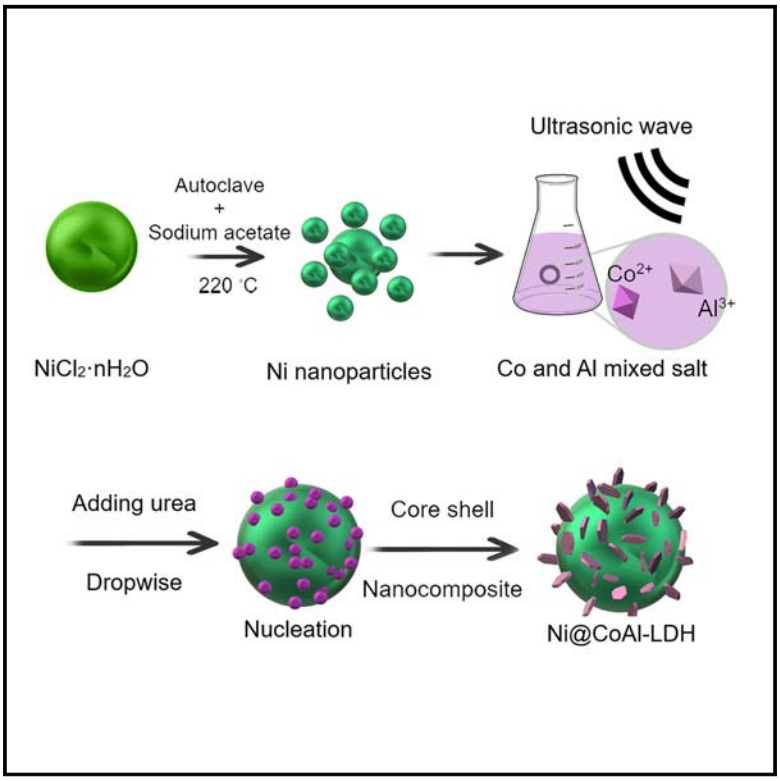

Authors

Edris Jamshidi, Samad Dalvand, Faranak Manteghi, Seyed Morteza Mousavi-Khoshdel

Correspondence

f_manteghi@iust.ac.ir

In brief

Chemistry; Electrochemical energy storage; Materials science

Highlights

- Synthesis of a Ni(0)@Co-Al LDH structure by a green method
- Using Ni(0) as a core structure to enhance the supercapacitive performance
- Adding spheres to platelet structures to resist harsh environments
- 3D flower-like, multilamellar morphology with enhanced electrochemical performance

Jamshidi et al., 2025, iScience *28*, 111672
February 21, 2025
https://doi.org/10.1016/j.isci.2024.111672

CellPress

iScience

CellPress
OPEN ACCESS

Article

A cobalt-aluminium layered double hydroxide with a nickel core-shell structure nanocomposite for supercapacitor applications

Edris Jamshidi,[1] Samad Dalvand,[1] Faranak Manteghi,[1,2,*] and Seyed Morteza Mousavi-Khoshdel[1]
[1]Department of Chemistry, Iran University of Science and Technology, Tehran 16846-13114, Iran
[2]Lead contact
*Correspondence: f_manteghi@iust.ac.ir
https://doi.org/10.1016/j.isci.2024.111672

SUMMARY

Layered double hydroxides (LDHs) are promising structures in applications including supercapacitors, which are claimed to help in arresting environmental chaos by their ability in energy storing. In this work, a Co-Al LDH and its metallic Ni core-shell nanocomposite were prepared and described using Fourier transform infrared (FTIR), X-ray diffractometer (XRD), scanning electron microscopy (SEM), and transmission electron microscopy (TEM) techniques. The two materials were electrochemically examined. The specific capacitance in current density of 1 A g^{-1} was 90 C g^{-1} (341.75 F g^{-1}) and 210 C g^{-1} (792.5 F g^{-1}) for the LDH and its composite, respectively. Compared with similar composites, the specific capacitance, especially the composite has a larger value in the order of 1.08–5.82 of magnitude. Moreover, the cycle stability test shows a slow drop at current density 4 A g^{-1} within 3,000 cycles, meaning that for the pure hydroxide and its Ni composite, a loss of 21% and 10% of specific capacitance was observed, respectively.

INTRODUCTION

In recent decades, clean, sustainable, and renewable energy has been at the center of due to the need to reduce environmental pollution carried on by fossil fuel combustion. Moreover, the application of modern digital communications and electric vehicles has led to an increasing demand for renewable energy-based devices. Thus, it is necessary to develop some efficient electrochemical energy conversion and storage devices. Therefore, some efficient electrochemical energy storage and conversion devices must be developed. Finding novel and renewable energy storage devices, which perform efficiently and conveniently has encouraged researchers to propose diverse devices with a wide range of properties.[1–4] Among these energy storage devices are supercapacitors (SCs), capacitors, lithium-ion batteries, and fuel cells.[5–8]

Supercapacitors (SCs), also referred to as electrochemical capacitors, are a novel class of power source with extended cycle life, high power density, and faster charging and discharging ability.[9,10] SCs are categorized as electric double-layer capacitors and pseudocapacitors relying on their charge storage mechanism.[11,12] The superior electrochemical capabilities of SCs are closely tied to their energy storage principles, which can be divided into two main categories. (1) The first mechanism entails the electric double-layer capacitor (EDLC). It operates by adsorbing ions onto the electrode surface without undergoing any chemical reactions. (2) The second mechanism recognized as pseudocapacitance entails swift redox reactions that take place at the electrode-electrolyte contact.[13,14]

EDLCs are designed and fabricated using two electrodes based on carbon materials, an electrolyte solution, and a separator. This system stores energy through electrostatic interaction between electrolyte ions situated on the electrode material surface. An EDLC SC may undergo more than 100,000 charge/discharge cycles without significant capacitance loss during the cycles, depending on the electrochemical characteristics and kinetics of the electrodes carbon nanotubes, activated carbon, graphene, mesoporous carbon, and reduced graphene oxide are examples of electrode materials that possess a unique structure, boasting large surface areas, exceptional chemical and mechanical stability, as well as outstanding electrical conductivity. These attributes make them highly sought-after choices as ideal electrode materials for EDLCs.[15,16]

Pseudocapacitors electrostatically store the charge through a faradaic process, wherein charge transfer occurs between ions, electrolytes, and electrode materials. Generally, pseudocapacitors exhibit superior specific capacitance and specific energy compared to EDLCs. Still, their charge/discharge rate is slower, and they exhibit significantly lower specific power performance and cyclic stability compared to EDLCs. Typical electrode materials encompass transition metal oxides, ionic liquids, and conducting polymers.[17,18] The mechanism of both types of SCs are given in Schemes 1 and 2.

Nonetheless, the comparatively low energy density of SCs while maintaining a high-power density continues to hinder their practical application. Therefore, the SC electrode materials should be modified to provide them the benefits of extremely high energy density and extremely long life.[19–21] Some of the

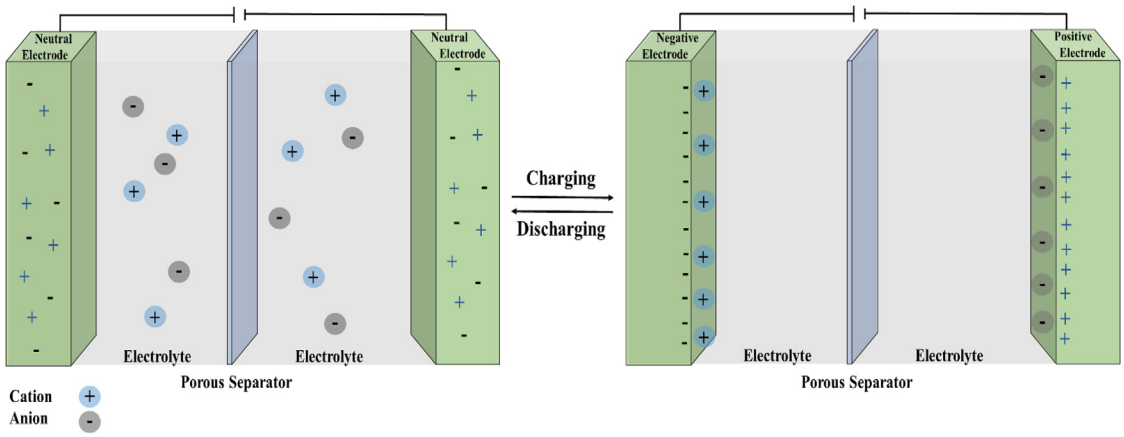

Scheme 1. Charge/discharge process of an EDLC supercapacitor
Reproduced with permission (study by He et al.[19]). Copyright 2018, Journal of Energy Storage.

most studied active pseudocapacitive materials are conducting redox polymers, transition metal oxides (RuO_2, Co_3O_4, and $NiCo_2O_4$), and hydroxides ($Ni(OH)_2$, $Co(OH)_2$) because of their significant electrochemical activity, and good pseudocapacitive performance.[12,22]

In recent researches, to explore the high-performance electrode materials for SCs, metallic layered double hydroxides (LDHs), which are known as a type of layered inorganic two-dimensional material, have aroused great interest in adsorption where charge-balancing anions are found between the layers and host layers contain divalent and trivalent metal cations. They are well applied in many applications including pollutant adsorption, sensors, composites, delivery of drugs, etc.[23–28] Additionally, It has been shown that LDHs, with their strong electrochemical activity, low cost, and adjustable composition, have great potential for advanced SCs.[29,30] Another limitation on the surface redox process of LDH nanosheets is the solid-state diffusion. Growing the interlayer gap between nanoplates is a viable and efficient way to accelerate and enhance kinetics. Novel nanostructures such as core-shell, nanowires, nanowalls, nanofilm, polymer-supported oxides/hydroxide hybrids, and so on are designed in order to improve the performance of the pseudocapacitive material. This tactic might accelerate mass transfer while also boosting electron transfer, resulting in favorable electrochemical characteristics.[16,18,31–33] In these nanostructure, higher efficiency and long cycle life are the outcome of a high energy density, high specific surface area, and elevated charge transfer rate. To achieve a long-lasting SC with high specific capacitance, the electroactive substance must bear additional species to take part in the faradaic redox reaction.[34–36]

In 2015, Tao and coworkers revealed a NiCo-LDH without the need for an oxidant, adscititious alkali source, or procedure to remove the SiO2 template. A 3D structure with a clearly defined hollow interior and hydrangea-like exterior is designed when the formation rate of NiCo-LDH nanoflakes and the template removal rate are closely matched. This allows for the transfer of electrons and mass during the faradaic redox reaction. The NiCo-LDH electrode demonstrated high electrochemical performance as a SC. At a current density of

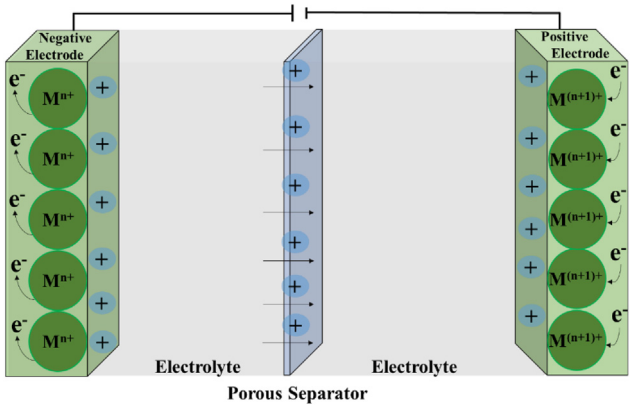

Scheme 2. Representative mechanism of a pseudocapacitor
Reproduced with permission (study by He et al.[20]). Copyright 2014, RSC Advances.

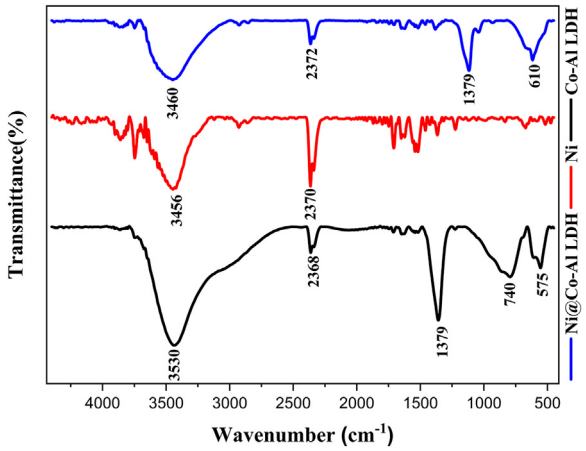

Figure 1. The IR spectra
Ni core (red, middle), CoAl-LDH (black, bottom), and the core-shell structure of Ni@CoAl-LDH (blue, top).

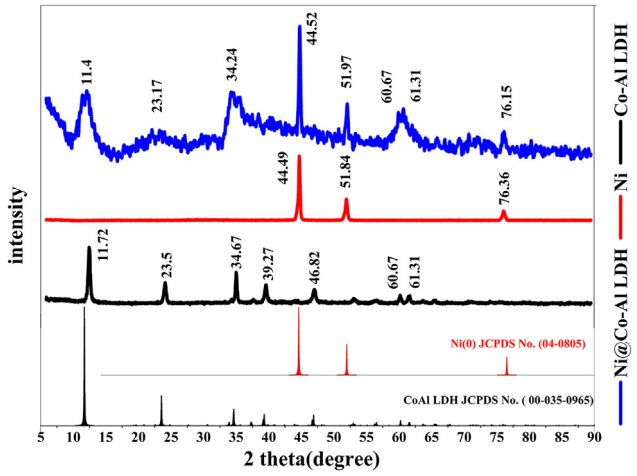

Figure 2. XRD patterns
CoAl-LDH (black, bottom), Ni nanoparticles (red, middle), and Ni@CoAl-LDH (blue, top).

1 A g^{-1} and 5 A g^{-1}, the specific capacitance can reach up to 2,158.7 F g^{-1} and 1,965.6 F g^{-1}, respectively, which can keep its capability after 1,500 cycles.[37] In another study, GS/NiCo-LDH (graphene sheets decorated with ultrathin nanoflakes of nickel-cobalt LDH) was proposed and showed excellent supercapacitive performances with the maximum specific capacitance equal to 1,980.7 F g^{-1} at the current density of 1 A g^{-1}. The authors claim that their study could provide a potential pathway for achieving metallic LDH/graphene hybrid materials with time- and money-saving qualities for energy conversion/storage applications.[38] Binder-free Co_3O_4@NiCoAl-LDH core-shell hybrid structural nanowire arrays were another choice that was synthesized by Li et al., in which due to the highly synergistic effect between the rigorous Co_3O_4 nanowire arrays and LDH nanosheets, Co_3O_4@LDH nanowire arrays with a 2–1.5 M ratio (Co_3O_4: LDH) demonstrated high specific capacitance (1,104 F g^{-1} at 1 A g^{-1}), adequate rate capability, and cycling stability (87.3% after 5,000 cycles).

Herein, we design a Ni@CoAl-LDH core-shell structure that is a novel core-shell structure with Ni(0) as core for the very first time, characterize and finally examine its electrochemical performance as a SC electrode and compare it with the CoAl-LDH

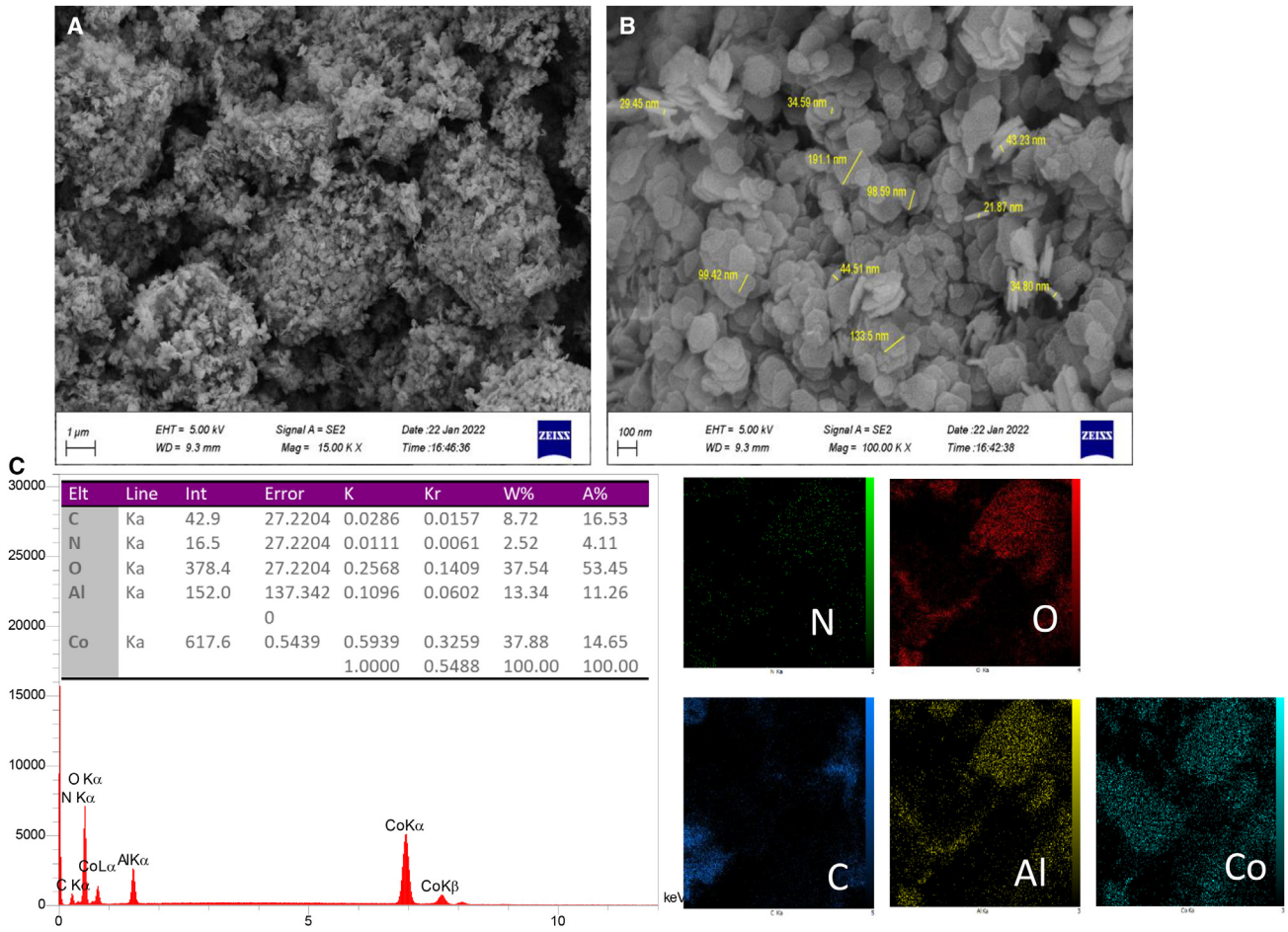

Figure 3. The LDH SEM and EDS analysis
The SEM images of CoAl-LDH (A and B), EDS analysis and elemental mapping of CoAl-LDH (C).

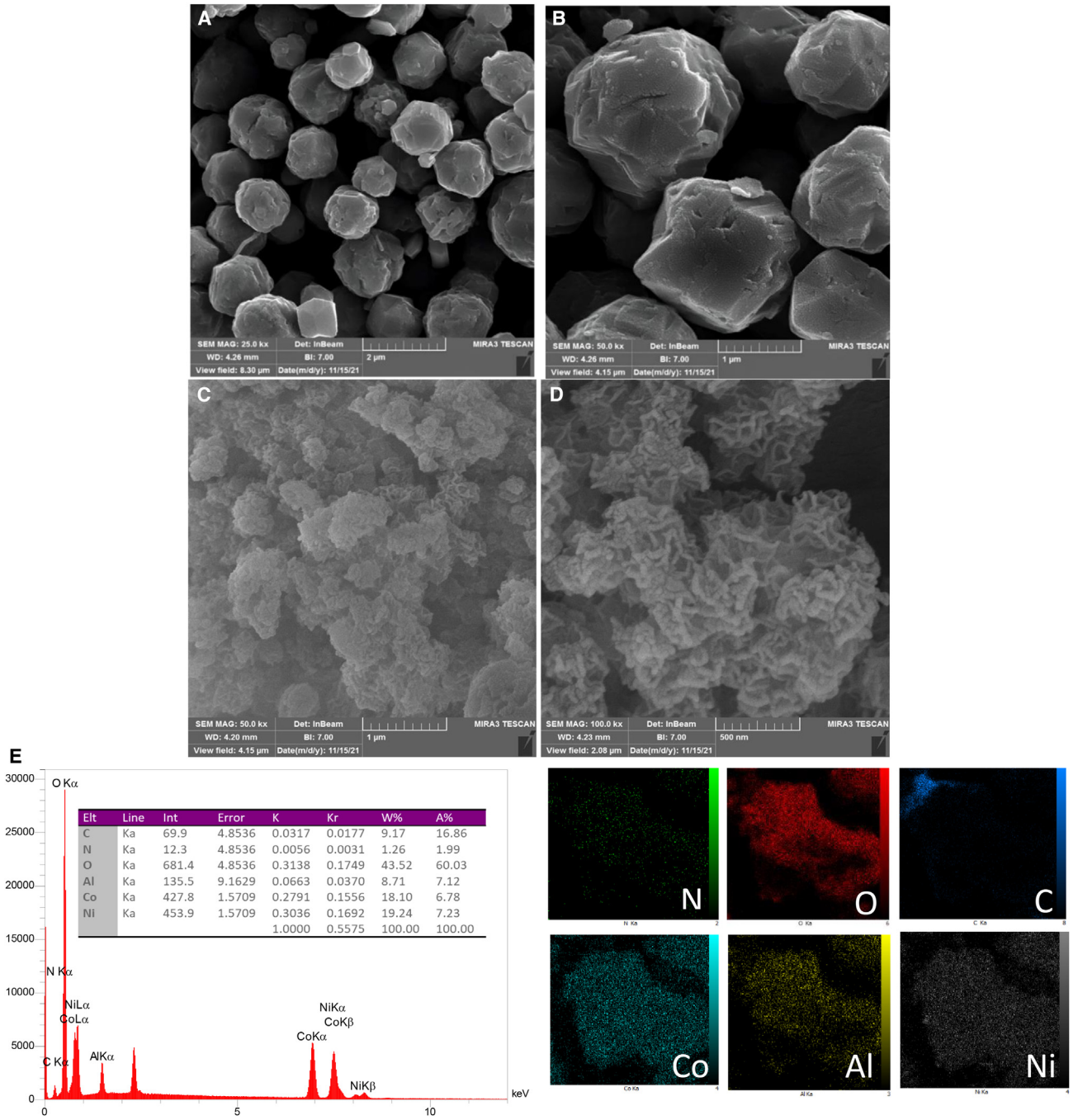

Elt	Line	Int	Error	K	Kr	W%	A%
C	Ka	69.9	4.8536	0.0317	0.0177	9.17	16.86
N	Ka	12.3	4.8536	0.0056	0.0031	1.26	1.99
O	Ka	681.4	4.8536	0.3138	0.1749	43.52	60.03
Al	Ka	135.5	9.1629	0.0663	0.0370	8.71	7.12
Co	Ka	427.8	1.5709	0.2791	0.1556	18.10	6.78
Ni	Ka	453.9	1.5709	0.3036	0.1692	19.24	7.23
				1.0000	0.5575	100.00	100.00

Figure 4. The core-shell structure SEM and EDS analysis

The Ni nanoparticles as core structure (A and B) and Ni@CoAl-LDH as core-shell structure (C and D) EDS analysis and elemental mapping of CoAl-LDH (E).

structure without any core and investigate the Ni(0) core effect on electrochemical performances.

RESULTS AND DISCUSSION

After preparing the three samples including Ni, CoAl-LDH, and Ni@CoAl-LDH, IR spectroscopy was applied to investigate the bonds and also the presence of components in the composite. As shown in Figure 1, the IR spectra contain a broadening characteristic signal at about 3460 cm^{-1} that is related to the –OH group's stretching vibration. In contrast, to clean Ni, peaks at 575 cm^{-1} and 740 cm^{-1} for Ni@CoAl-LDH and CoAl-LDH are ascribed to Co–O and Al–O stretching vibrations, respectively. The peaks that appeared at 1,379 cm^{-1} refer to interlayer NO_3^-

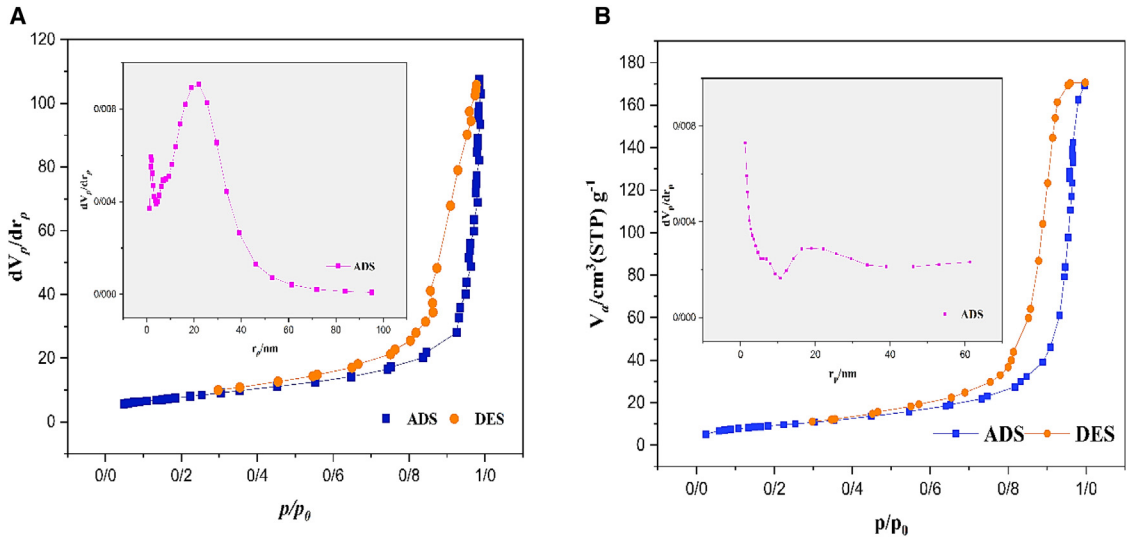

Figure 5. BET analysis

The N2 adsorption-desorption isotherms and pore-size distribution (inset) of the CoAl-LDH (A) and Ni@CoAl-LDH (B).

anions. In the spectrum of Ni@CoAl-LDH, the peak at 1,190 cm^{-1} points to the C−O bonding of the remaining sodium acetate. Water molecules were observed at a peak with 3,530 cm^{-1} wavelength.[39]

Another applied method of characterization was X-ray diffractometer (XRD) shown in Figure 2, in which the black (bottom) pattern refers to CoAl-LDH, and presents the complete growth with good crystallinity of LDH sheets. The two sharp peaks at 2θ 11.72 and 23.5, are related to (003) and (006) planes, respectively. The peaks at 2θ 34.67, 39.27, and 46.82 are corresponding to (012), (015), and (018) planes, respectively. Finally, two peaks at 2θ 60.67 and 61.31 refer to (110) and (113) planes, respectively (JCPDS card No. 51-0045). As can be seen in the pattern of Ni(0), the strong peaks at 2θ 44.49, 51.84, and 76.36 are related to (111), (200), (220) planes of metallic Ni, respectively (JCPDS card No. 7440-02-0) also can be found in the pattern of Ni@CoAl-LDH.[40] However, the strong peak at 2θ 11.4 and a broad peak at 23.17 of Ni@CoA-LDH are attributed to (003) and (006) planes of CoAl-LDH, and the twin peaks at 2θ 60.67 and 61.31 referred to (110) and (113) planes, respectively.

The scanning electron microscopy (SEM) images represented in Figures 3A and 3B demonstrate that the LDH sheets were prepared successfully and as it turns out, the LDH sheets reached their maximum growth in size. SEM images of Ni(0) core and Ni@CoAl-LDH core-shell structures were also provided in Figures 4A and 4B. The images depict that the Ni core structures were successfully synthesized using the hydrothermal process, the uniform contribution and relatively circular form of the as-prepared core has been confirmed by SEM technique, as illustrated in Figures 4A and 4B. The Ni@CoAl-LDH core-shell composite has been synthesized through the sonication-urea method, as displayed in Figures 4C and 4D, it has a flower-like multi-lamellar morphology of the CoAl-LDH shell, which coats the Ni core, thoroughly.

In the energy-dispersive X-ray (EDS) spectrum of Figure 3C, the successful synthesis of the LDH is confirmed by the distinct peaks of N, C, Co, Al, and O. The elemental mapping nanographs of oxygen, aluminum, carbon, nitrogen, and cobalt in CoAl-LDH are displayed in Figure 3C, confirming the elements' even distribution throughout the LDH structure. The EDS profile of Ni@CoAl-LDH (Figure 4E), also demonstrates the existence of proportion to the original ingredients utilized in Ni@CoAl LDH composite. The elemental mapping verifies the homogeneous distribution of Al, Co, Ni, N, O, and C elements across the LDH core-shell structure in the Ni@CoAl LDH. Moreover, the presence of carbon and nitrogen is related to the CO_3^{2-} and NO_3^- anions within the CoAl-LDH sheets. The Ni@CoAl-LDH composite has 19.24 wt. % Ni, 18.10 wt. % Co, 7.48 wt. % Co, 8.71 wt. % Al, and 43.52 wt. % O, according to quantitative analysis. As well as 37.88 wt % Co, 13.34 wt % Al, and 37.54 wt % O, only in CoAl-LDH, which exhibits a suitable correlation with the values employed in the synthesis approach.

The ion dispersion of the material will be influenced by factors such as specific surface area, pore size, and pore volume. Consequently, CoAl-LDH and Ni@CoAl-LDH materials underwent Brunauer-Emmett-Teller (BET) analysis; the conclusions are presented in Figures 5A and 5B, respectively. As can be seen, the two sets of adsorption and desorption curves fit into type IV isotherms, suggesting that mesoporous materials play a major role in the adsorption process.[41] The significant parameters of the BET results are summarized in Table 1.

Pore size distribution profiles in Figure 5 calculated by the Barrett-Joyner-Halenda (BJH) method are bimodal and consistent with the mesoporous nature of the samples.[42] Pore size distributions (PSD) of Ni@CoAl-LDH and CoAl-LDH are between 1 and

Table 1. Parameters of the BET results

Sample	BET surface area (m^2 g^{-1})	Pore volume (cm^3 g^{-1})	Pore size (nm)
CoAl LDH	49.23	0.25	23.76
Ni@CoAl LDH	81.14	0.46	30.19

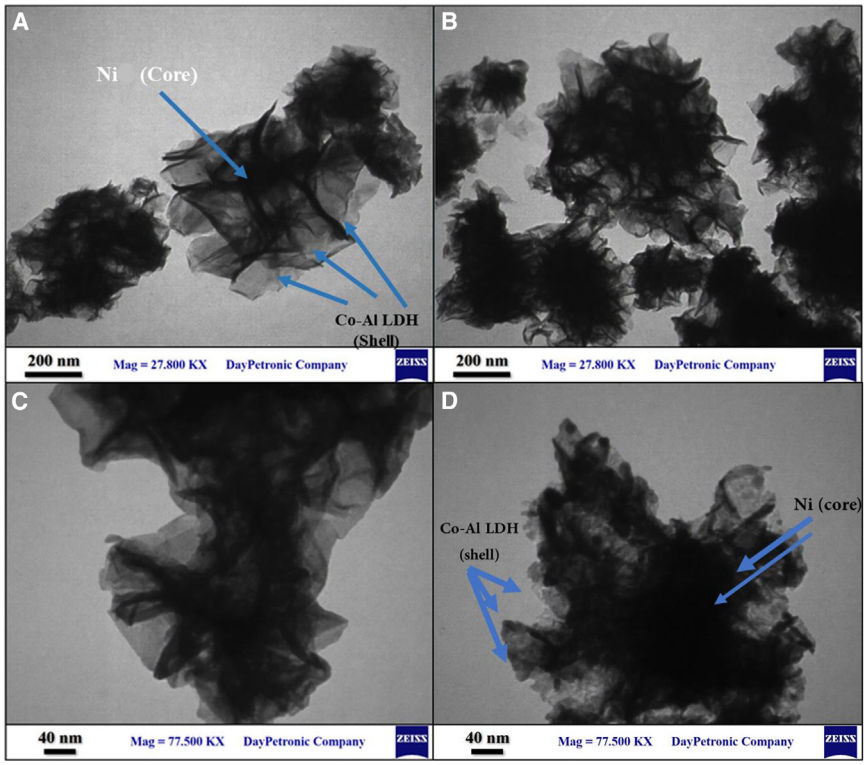

Figure 6. TEM images

(A–D) The Ni@CoAl-LDH as-prepared TEM images with different magnifications, scales, and views.

25 nm. In addition, the PSD curves of the two materials show a maximum volume distribution at 1–3 and 15–25 nm. The Ni@CoAl-LDH composite's porous structure makes it capable of exposing more active sites during the electrochemical.

The Ni@CoAl-LDH composite's as-prepared transmission electron microscopy (TEM) images were illustrated in Figures 6A–6D. As can be observed, CoAl-LDH grew on the Ni core, completely as a shell structure. In the TEM images, the Ni dark cores and semi-transparent sheets as CoAl-LDH shells are well-defined. The arrows indicate Ni cores and Co-Al shells. Figures 6A and 6C display hexagonal sheet-like morphology with the single-platelet thickness of LDH. The TEM image revealed clear lattice fringes that corresponded to the CoAl-LDH phase's (110) crystal plane. In Figure 2, including the XRD patterns of the materials, the peaks related to LDH in the Ni@CoAl LDH pattern (blue), have a lower intensity and got wider than the same peaks related to the CoAl-LDH. The LDH platelets may break into smaller ones during the sonication and stirring process, because of the layer breakdown that occurred. MgAl-LDH layer behavior was reported to be similar,[43] or the sheets could not reach the maximum size and they grew to half size due to the limitation of the urea synthesis method. The most plausible reason for the decrease in platelet size could be due to the brittle character of the LDH nanoparticles.

Electrochemical measurements

An electrochemical workstation was used to test the prepared working electrodes' electrochemical performance (Autolab model PGSTAT204). Using a three-electrode setup, the prepared samples were evaluated. As shown in Scheme 3, the electrode material was made by combining carbon black, polytetrafluoroethylene (PTFE), and active materials powder in an N-methyl-2-pyrrolidone (NMP) solution at a weight ratio of 80:5:15. The mixture was then applied on nickel foam sized 1 cm by 1 cm.[44] In a 1 cm^2 area, the coated material mass was approximately 3 mg.

The coated nickel foam, platinum, and Ag/AgCl were used as the working electrode, counter electrode, and the reference electrode in a 1 M KOH solution as an electrolyte, respectively. Autolab model PGSTAT204 was used to measure all electrochemical tests, such as potentiostat/galvanostat (GCD), cyclic voltammetry (CV), and electrochemical impedance spectroscopy (EIS). The EIS test was performed at open circuit potential with an AC perturbation of 0.29 V, covering the frequency range of 0.01 Hz–100 kHz Equation 1 was applied to calculate the specific capacitance of the prepared electrode by using the charge/discharge curves.

$$C_S = \frac{I \times \Delta t}{m \times \Delta V} \quad \text{(Equation 1)}$$

where C_S (F g^{-1}), I (A), Δt (s), ΔV (V), and m (g) are the specific capacitance, charge/discharge current, discharge time, potential window, and total mass of the electrode materials, respectively.[45]

Electrochemical and super capacitive performance

The typical cyclic voltammetry the performances of the Ni@CoAl-LDH and CoAl-LDH electrodes were examined at various scan rates in an aqueous solution of 1 M KOH. The Co-Al-LDH and Ni@CoAl-LDH CV curves are shown in Figure 7 at scan rates of 2, 5, 10, and 50 mV/s in the potential window range of 0.2–0.6 V.[46] It is evident that the curve exhibits two prominent redox peaks, a consequence of the enhanced pseudocapacitive characteristic attained by the observation of redox reactions, in which cobalt hydroxide first converts to cobalt oxyhydroxide and then changes to cobalt peroxide.[47]

$$Co(OH)_2 + OH^- \leftrightharpoons CoOOH + H_2O + e^-$$

$$CoOOH + OH^- \leftrightharpoons CoO_2 + H_2O + e^-$$

Moreover, the Al^{3+} ion is not electroactive over the redox reaction. Al^{3+} ions will alter Co^{2+} to Co^{3+} due to distorting the octahedral symmetry of the ligands around cobalt ions.[48] Taking into account that Al^{3+} is present in LDHs, which aim to boost charge

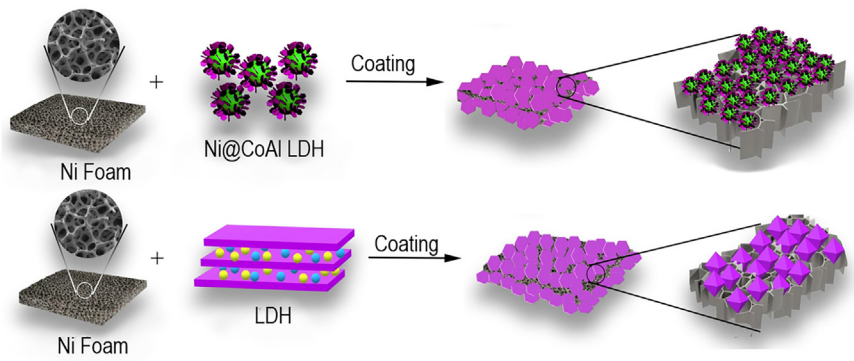

Scheme 3. The two procedures of electrode preparation by depositing on Nickel foam
LDH (A) Ni@CoAl-LDH (B).

transport and electrolyte efficiency, the hydrophilicity and the crystallinity of LDHs can be enhanced.[49]

The anodic peak at around 0.6 V and a cathodic peak at approximately 0.2 V are the only two strong redox peaks identified. These distinct peaks with good width and intensity also point to a high specific pseudocapacitance and faradic reaction. Between 2 and 50 mV/s, there is almost no intrinsic shape change seen in these CV curves indicating excellent reversibility and stability of electrode material. The reason that peak intensities rise as scan rates rise is that the square root of the scan rate and current intensity are directly correlated. Furthermore, when it comes to high-current charge/discharge, a tiny peak-to-peak separation frequently indicates a rapid electron transfer behavior.

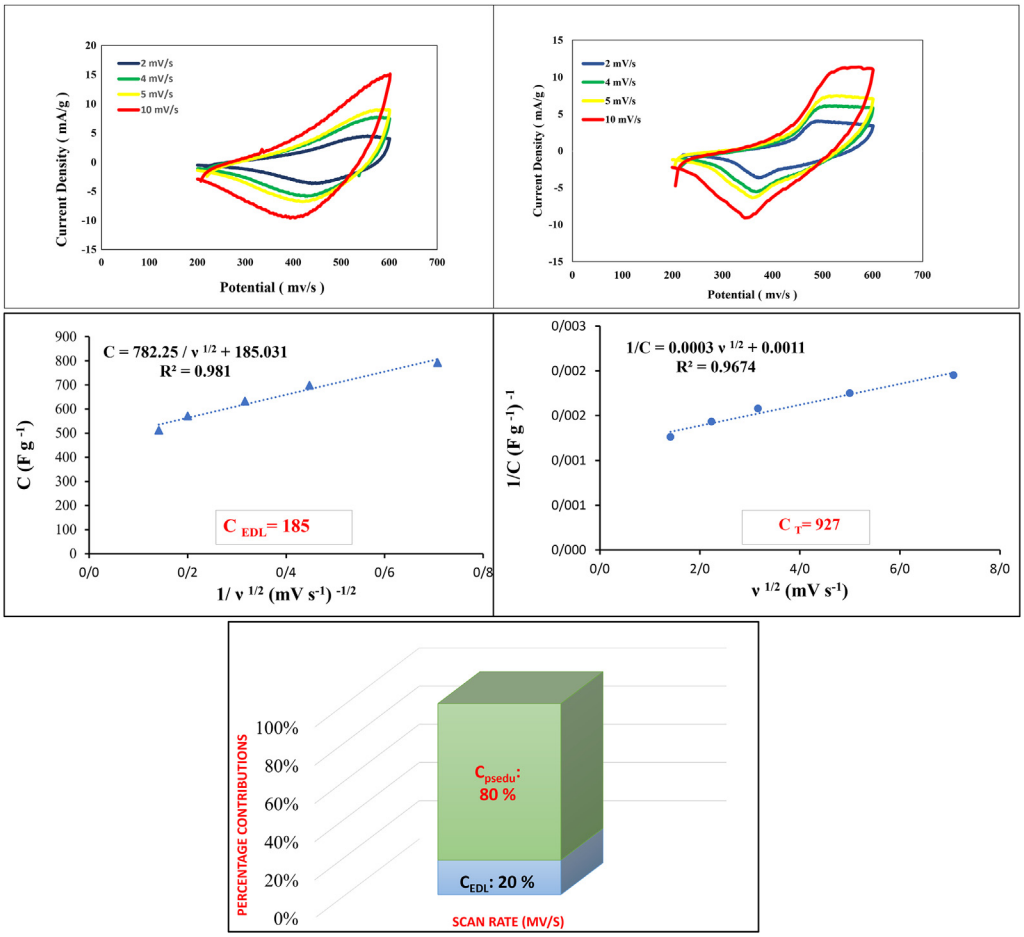

Figure 7. Electrochemical analysis 1
(A and B) CoAl-LDH (A) and (B) Ni@CoAl-LDH cyclic voltammetry curves, at the scan rates of (2, 5, 10, 50) mV s^{-1}.
(C) Plot showing C against the scan rate's inverse square root.
(D) Plot showing C vs. scan rate's square root.
(E) EDL pseudocapacitance and capacitance percent were estimated by the Trasatti method.

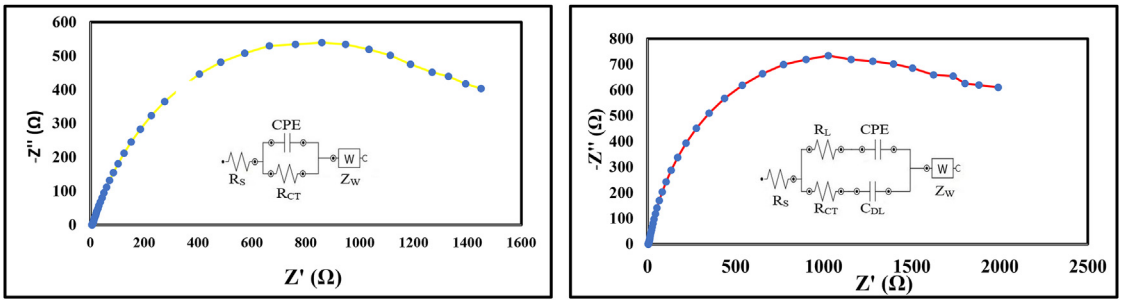

Figure 8. EIS analysis
(A) CoAl LDH and (B) Ni@CoAl LDH electrodes Nyquist plots.

In an electrochemical system, devolution of double-layer capacitance's (C_{EDL}) contribution from pseudocapacitive (C_{Pseudo}) capacitance is a primary issue exhibiting pseudocapacitance behavior. To accomplish this, the Trasatti method that assumes semi-infinite ion diffusion was used, to further study the CV curves collected at various scan rates. The specific capacitance (Cs) quantities for each scan rate (v) were first determined. In the next step, the intercepts of the following equations were used to calculate the total capacitance (C_T) and C_{EDL}, respectively:

$$C = C_{EDL} + \frac{constant}{\nu^{1/2}} \quad \text{(Equation 2)}$$

$$\frac{1}{C}\frac{1}{C_T} + constant\ \nu^{1/2} \quad \text{(Equation 3)}$$

Furthermore, by subtracting electric double-layer capacitance from total capacitance, the value of C_{pseudo} could be estimated. In light of Figures 7C and 7D, C_{Edl}, C_T, and C_{Pseudo} values were found to be 185, 927, and 742, respectively. Thus, approximately 86% of the total capacitance was attained as the pseudocapacitance contribution. (Figure 7E).

The evaluation of charging kinetics concerning capacitive behavior was done using EIS. Moreover, it was used to analyze the electrodes and electrolytes resistance. The Nyquist plots of CoAl-LDH and Ni@CoAl-LDH materials at 0.01 Hz to 100 kHz of the frequency range, and in 0.29 V of open circuit potential (OCP) were provided in Figure 8 In the experimental condition, In the Nyquist plot, two semicircles should generally be seen, which the former is credited with solution resistance and charge transfer resistance (R_{CT}) in the high frequency region of the CoAl-LDH electrode and the latter is related to the low-frequency region of constant phase element (C_{PE}) of pseudocapacitance and Warburg resistance (Z_W).

Table 2. Impedance parameters after fitting derived from the equivalent circuit

	R_S (Ω)	R_{CT} (Ω)	C_{PE} (F)	Z_W		
CoAl-LDH	3.198	1266.5	0.0007	0.0064	–	
Ni@CoAl-LDH	R_S (Ω)	R_{CT} (Ω)	R_L (Ω)	C_{PE} (F)	C_{DL} (F)	Z_W
	107.14	685.75	88.811	0.0015	1.1×10^{-6}	0.0055

In the case of Ni@CoAl-LDH electrode, the first semi-circle is contributed to the high frequency region of solution resistance, charge transfer resistance (R_{CT}), and double layer capacitance (C_{DL}), while the second semi-circle is related to low-frequency region of leakage resistance (R_L), constant phase element (C_{PE}) of pseudocapacitance and Warburg resistance (Z_W). As the curves in Figures 8A and 8B and shown by the results of Table 2, the charge transfer resistance for Ni@CoAl-LDH is less than that of CoAl-LDH. This leads to an increase in ions diffusion from the electrolyte solution toward the surface of the electrode, improving electrochemical performance (energy density specific, capacitance, power density, etc.). The electrical circuits and their parameters are provided in the Nyquist plot of Figure 8 and Table 2.

To provide more insight into the electrochemical performance of the product, the final materials were designed as SC electrodes, and galvanostatic charge/discharge measurements were employed to characterize by. Figure 9 shows the first discharging curves of Ni@CoAl-LDH and CoAl-LDH electrodes in 1 mol L^{-1} KOH in the 200–600 mV s^{-1} potential range at 1, 2, 3, 4, and 5 A g^{-1} current densities. It is obvious that the diagrams display redox peaks, in both samples are accordant with the CV curves. It could be concluded that the electronic materials have pseudocapacitive behavior.

The peaks' constancy in high current densities is related to electrochemical performance and material fast kinetics. As is clear, the Ni@CoAl-LDH exhibits a much longer discharge period and higher specific capacity in comparison to the Co-Al-LDH without a Ni core. The Ni@CoAl-LDH represents the highest possible specific capacitance up to 792.5 F g^{-1} at 1 A g^{-1} current density, much higher than the results of CoAl-LDH (341.75 F g^{-1}).

Three factors contribute to the Ni@CoAl-LDH nanocomposite's high capacitance. First off, Ni spheres can serve as an excellent platform for Ni@CoAl-LDH nanosheets' conductivity, enhance the potential for electron transfer, and encourage the ion's oxidation-reduction reaction on the electrode surface. Second, Ni spheres can inhibit Ni@CoAl-LDH's accumulation, expand the electrode material's specific surface area, amplify the electrolyte and electrode material contact, and boost the active material's efficiency of utilization. Lastly, CoAl-LDH and Ni spheres come together to form a three-dimensional spherical

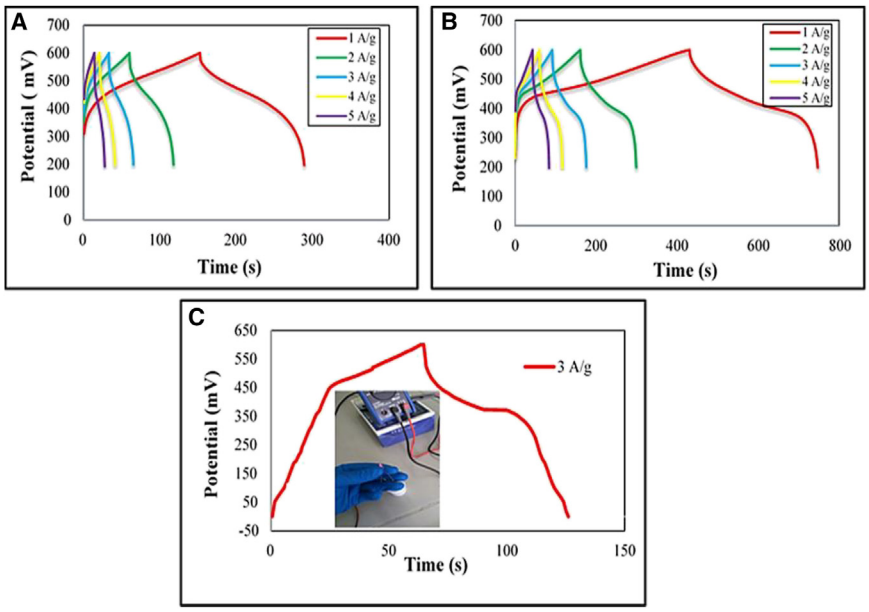

Figure 9. Electrochemical analysis 2

(A) CoAl-LDH and (B) Ni@CoAl-LDH electrodes' galvanostatic charge and discharge curves at various current densities (C) charge/discharge curve of the symmetric device at 3 A g^{-1} current density, with the inset picture showing illuminated a 1.2 V LED for 2 min with a charge potential of 0.6.

structure that leads to boosting the durability of synthetic structures, intended to enhance the electrode material's cycle and rate performance.

The electrode material's specific capacitance decreases progressively as the current density rises from 1 A g^{-1} to 5 A g^{-1} (Figures 9A and 9B). It is possible to conclude that the electrode material's effective surface area is adequate for the redox reaction at a lower current density. A reduced specific capacity is the result of insufficient contact between the electrolysis liquid ions and the electrode's active surface as the current density rises.[47]

Eventually, a two-electrode device charge/discharge at 3 A g^{-1} current density was estimated as displayed in Figure 9C. Furthermore, the specific energy and specific power (performance of energy storage) was achieved utilizing the corresponding relationships shown in the following, respectively:

$$E = \frac{C \times \Delta V^2}{7.2} \quad \text{(Equation 4)}$$

$$P = \frac{E \times 3600}{\Delta t} \quad \text{(Equation 5)}$$

where Cs, V, and t are specific capacitance (F g^{-1}), potential drop during discharge (V), and discharge time (s), respectively.

Table 3. The sample's specific capacitance at various current densities

	Current density (A g^{-1})	1	2	3	4	5
CoAl-LDH	C (F g^{-1})	341.75	287	240.75	203	173.75
Ni@CoAl-LDH	Current density (A g^{-1})	1	2	3	4	**5**
	C (F g^{-1})	792.5	697.5	632.25	571	512.5

Figure 9C illustrates how the 2-electrode device set up in 1 M KOH electrolyte generated specific energy and specific power of 15.5 Wh kg^{-1} and 900 W kg^{-1}.

As shown in Table 3, the specific capacitance values for the single LDH sample are 341.75, 287, 240.75, 203, and 173.75 F g^{-1}, respectively, at 1, 2, 3, 4, and 5 A g^{-1}. Likewise, values of the Ni@CoAl-LDH's capacitance at 1, 2, 3, 4, 5 A g^{-1} is 792.5, 697.5, 632.25, 571, 512.5 F g^{-1}, respectively. The insertion of core-shell structure is seen to significantly improve the capacitance of Ni@CoAl-LDH.

This demonstrates that because of its distinct 3D nanonetwork morphology, Ni@CoAl-LDH exhibits improved capacitance rate performance. The samples' specific capacitances at various current densities are displayed in Table 3. Based on the obtained results, the rate capability of Ni@CoAl-LDH electrode was estimated to be around 63% (Figure 10A) that makes sense for systems having the characteristics of pseudocapacitance. Furthermore, Table 4 presents a comparison of specific capacitance between Ni@CoAl-LDH electrodes with that of other comparable electrode materials. Compared to several of the published electrode materials, the Ni@CoAl-LDH nanocomposite has a greater specific capacitance. One of the most important key spots in practical application for SCs is cyclic stability. That is when an electrode is charged and discharged in consecutive cycles, how much it maintains its initial capacitance. As illustrated in Figure 10, cyclic stability was examined for both samples CoAl-LDH and Ni@CoAl-LDH by galvanostatic charge/discharge 5,000 tests at 4 A g^{-1} current density. It is evident that the Ni@CoAl-LDH sample has much better cycle stability. Within 5,000 cycles, a slow reduction in the specific capacitance is detected. For the pure LDH, there is a 22% loss presented. However, for the Ni@CoAl-LDH, the loss of 11% after the 5,000 cycles test is observed, in other words, both electrode materials have shown high stability in consecutive charge-discharge cycles, so the pure LDH maintained 78% of its capacitance and the core shell structure maintained 89% after 5,000 charge-discharge cycles.

In an ideal situation, coulombic efficiency is 100%, although as Figures 10B and 10C indicates, the coulombic efficiency for CoAl-LDH and Ni@CoAl-LDH is 199% and 205%, respectively. These values, which exceed 100%, indicate that there are significant side reactions occurring during the cycling tests. Such high coulombic efficiencies suggest that, in addition to the primary redox reactions, there might be contributions from parasitic

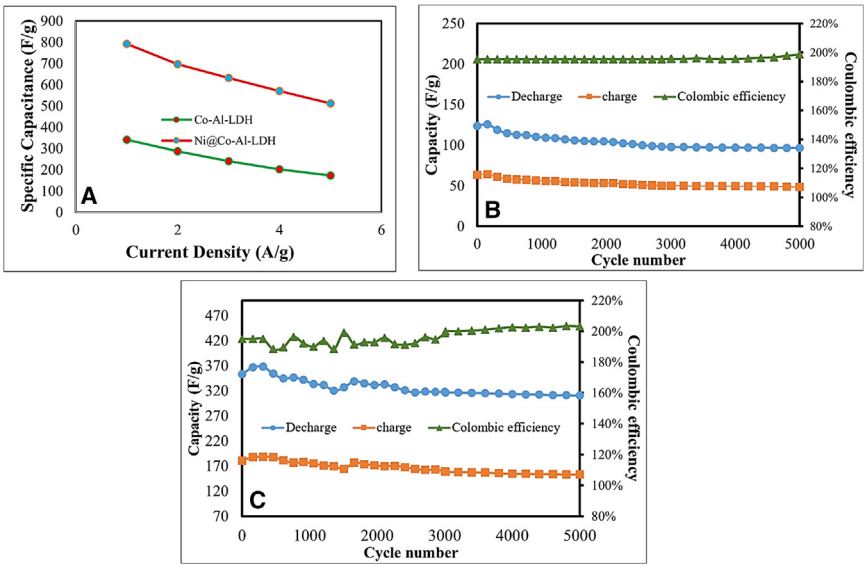

Figure 10. Cyclic stability measurements

(A) Specific capacitance variation versus current density for both CoAl-LDH and Ni@CoAl-LDH electrodes.

(B and C) The cyclic stability of CoAl-LDH and Ni@CoAl-LDH electrodes at a current density of 4 A g^{-1}.

reactions or leakage currents. These side reactions can be associated with the electrolyte decomposition, structural changes in the electrode materials, or other faradaic processes that do not contribute to energy storage.

While the Ni@CoAl-LDH electrode shows slightly better performance in terms of coulombic efficiency compared to CoAl-LDH, both materials demonstrate robust cyclic stability over 5,000 cycles. The irregular fluctuations in Figure 10C are likely due to the combination of morphological degradation, loss of crystallinity, and inherent electrochemical instability of the Ni@CoAl-LDH electrode material during prolonged cycling tests.

To determine the cause of the LDH electrodes' high specific capacitance and excellent stability performance, after 5,000 cycles of the charge-discharge procedure, SEM and XRD were used to characterize the electrode samples. SEM studies of CoAl-LDH and its Ni composite electrodes after 5,000 cycles indicate the existence of the nanosheet morphologies for the CoAl LDH (Figures 11A and 11B) but it should be noted that the sheets became more amorphous and lost their ordered hexagonal and sequin-like shape. As presented in Figures 11C and 11D, the Ni@CoAl-LDH indicates similar morphology, as those before the cycling test. Ni@CoAl-LDH preserved its core shell flower-like structure and no change was observed in SEM images.

Following the cyclic stability test, the electrodes' XRD patterns are shown in Figure 11E. The CoAl-LDH electrode's peaks

Table 4. Comparative electrochemical performances of different electrode materials for supercapacitor applications

Electrode materials	Electrolyte	Specific capacitance	Power Density	Energy Density	Cyclic stability	Reference
FeCo-LDH@C_3N_4	1 M HCl	593 F g^{-1} at 1 A g–1	–	–	83.72% after 10,000 cycles	Ma et al.[50]
Ni_3S_2@NiCo-LDH	PVA/KOH	1822 F g^{-1} at 5 mA g^{-1}	3.99 mW cm^{-2}	450.60 μW h cm^{-2}	85.2% after 5,000 cycles	Hu et al.[51]
NiCo-LDH NFs@$Co(OH)_2$	2 M KOH	858.9 F g^{-1} at 0.5 A g^{-1}	–	–	83.7% after 5,000 cycles	Zhai et al.[52]
NiCo-LDH/ZnO/CC	1 M KOH	1577.6 F g^{-1} at 1 A g^{-1}	800 W kg^{-1}	51.39 Wh kg^{-1}	87.3% after 1,000 cycles	Xiong et al.[53]
CNTs/CoNiFe-LDH	1 M KOH	176 mAh g^{-1} at 1 A g^{-1}	750.5 W kg^{-1}	29.9 W h kg^{-1}	85% after 3,000 cycles	Wang et al.[54]
Ce-Doped NiCo-LDH@CNT	6 M KOH	187.2 F g^{-1} at 1 A g^{-1}	–	–	85.6% after 9,000 cycles	Dinari et al.[55]
CuO@CoNi-LDH	6 M KOH	319.4 mAh g^{-1} at 1 A g^{-1}	400 W kg^{-1}	92.5 Wh kg^{-1}	83.3% after 8,000 cycles	Chen et al.[56]
CoAl-LDH/MWNTs	1 M NaOH	342.4 at 2 A g^{-1}	–	–	–	Su et al.[57]
CoAl-LDH@PEDOT	6 M KOH	672 at 1 A g^{-1}	13 kW kg^{-1}	39.4 Wh kg^{-1}	71% after 3,000 cycles	Han et al.[58]
CoAl-LDH/Pt	2 M KOH	734 at 1 A g^{-1}	750W kg^{-1}	25.5Wh kg^{-1}	50% after 6,000 cycles	Cheng et al.[59]
G/PANI/MCM-41	1 M Na_2SO_4	405 at 0.8 A g^{-1}	–	–	92% after 2,000 cycles	Sawangphruk et al.[60]
Fe_3O_4/C nanocomposite	1 M Na_2SO_4	136.2 at 1 A g^{-1}	705.5 W kg-1	27.2 Wh kg^{-1}	–	Sinan et al.[61]
CoAl-LDH	1 M KOH	341.75 at 1 A g^{-1}	–	–	78% after 5,000 cycles	This work
Ni@CoAl-LDH	1 M KOH	792.5 at 1 A g^{-1}	900 W kg^{-1}	15.5 Wh kg^{-1}	89% after 5,000 cycles	This work

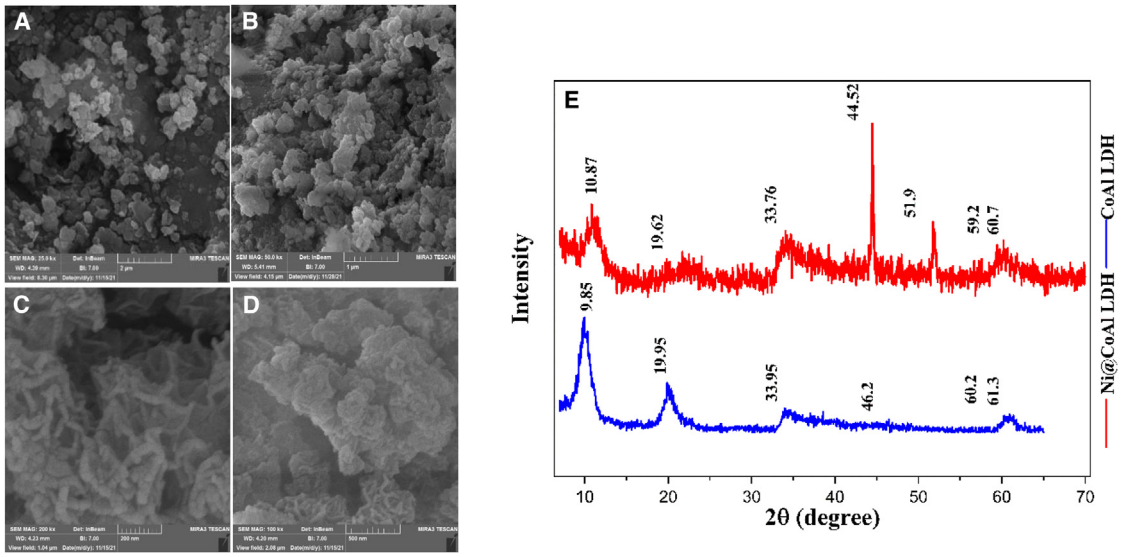

Figure 11. SEM images

SEM images of CoAl-LDH (A and B) and Ni@CoAl-LDH electrodes (C and D), and XRD patterns of CoAl-LDH and Ni@CoAl-LDH electrodes (E) after 5,000 cycles of charge/discharge.

widened and lost intensity in comparison to before the stability test. The results show that following the stability test, the degree of crystallinity has decreased. Furthermore, the XRD peaks shift backward at the lower diffraction angles implying that the interlayer spacing (d003) increases after the charge/discharge process. The core-shell LDH electrode provided comparable outcomes as well (shown in Figure 11, upper [red] pattern), but the peaks related to the Ni Core did not change, it can be concluded that nickel, despite its presence in the electrochemical reaction, exhibited good resistance against charge/discharge cycling stability effect.

In a literature survey, we found out that some composite structures containing CoAl-LDH and also other LDHs and their composites as component can be effective capacitors with different specific capacitances reported in Table 4.

As given in Table 4, Ni@CoAl-LDH with 792.5 F g^{-1} has the greatest amount of specific capacitance compared with other similar composites. This can be caused by synergistic effect of Ni and CoAl-LDH. In SCs as electrochemical energy storage devices, the higher the surface area of electrode, the higher the storage of energy. Therefore, this can be achieved by increasing the surface area in core-shell structure of the composite.[62]

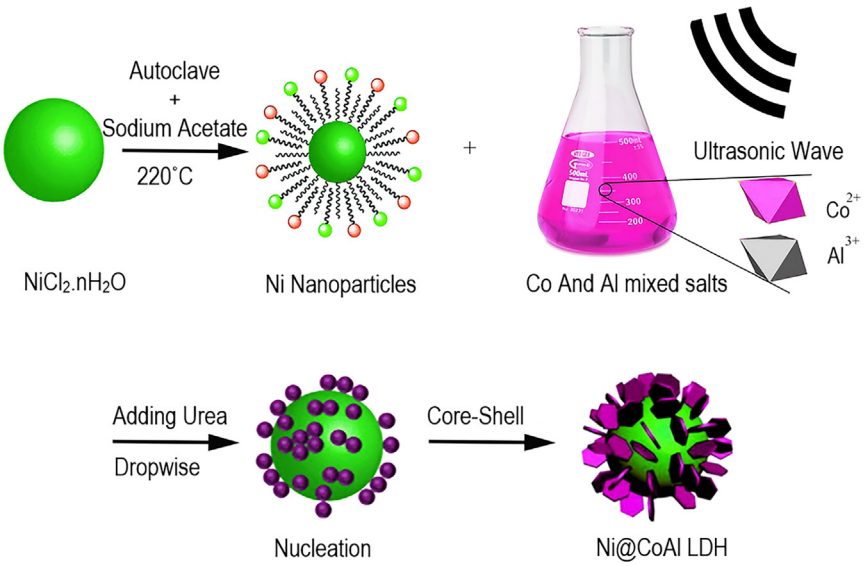

Scheme 4. The preparation procedure of Ni@CoAl-LDH

Conclusion

In this research, the electrochemical performance of a bimetallic LDH and its core-shell nickel nanocomposite was investigated. Compared with other composites, although the CoAl LDH shows a less or more specific capacitance, which in current density of 1 A g^{-1} is 90 C g^{-1} (341.75 F g^{-1}), its nickel composite has an apparently larger specific capacitance of 210 C g^{-1} (792.5 F g^{-1}). This enhanced performance of the nanocomposite can be explained by nickel's existence as a component and its synergistic effect with the other components. Conversely, however, its core-shell structure causes a high specific surface area providing suitable sites for better charge transfer.

In a detailed view, suitable capacitance of the composite arises from (1) Ni spheres that are good substrates for the conductivity of composite nanosheets, enhance the electron transfer capacity and facilitate redox of ion on the electrode surface; (2) Ni spheres, which can prevent the accumulation of Ni@CoAl-LDH, expand the electrode material's specific surface area, increase the contact of electrolyte and electrode material, and enhance the active material efficiency utilization; and (3) the core-shell structure that forms a 3D spherical structure, which helps to improve the composite material's stability, to enhance the nanocomposite's cycle and rate performance. The last word is about the innovation of the work which can be described in three parts. First is application of a nanocomposite, containing a metallic part and a LDH in an electrochemical process. Second is the core part consisting of Ni(0) synthesized by a green and sustainable method, instead of the most reported compound iron oxide, The third is ammonia and ethylene glycol, which are more moderate, safe and sustainable materials than NaOH, KOH, and ethanol, the common utilized alkalies and solvent, applied in the LDH synthesis procedure.

Limitations of the study

Due to limitations in the equipment available to us at this time, we were unable to conduct additional materials characterization, such as X-ray photoelectron spectroscopy (XPS), SEM-HAADF, and scanning transmission electron microscopy (STEM) analyses.

RESOURCE AVAILABILITY

Lead contact

Further information and requests for resources should be directed to and will be fulfilled by the lead contact, Dr. Faranak Manteghi, corresponding author (email: f_manteghi@iust.ac.ir).

Materials availability

The only material generated in this study was Ni^0@CoAl-LDH which was prepared in our laboratory according to the experimental section and illustrated briefly in Scheme 4.

Data and code availability

- All data reported in this paper will be shared by the lead contact upon request.
- This paper does not report original code.
- Any additional information required to reanalyze the data reported in this paper is available from the lead contact upon request.

ACKNOWLEDGMENTS

Authors are gratefully appreciating Iran University of Science and Technology for supporting this work.

AUTHOR CONTRIBUTIONS

EJ: conceptualization, methodology, software, validation, formal analysis, data curation, writing – original draft, writing – review & editing. SD: methodology, software, validation, formal analysis, data curation, writing – original draft, writing – review & editing. FM: conceptualization, methodology, validation, formal analysis, investigation, resources, writing – review & editing, visualization, supervision, project administration, funding acquisition. SMMK: software, formal analysis, visualization, supervision, project administration, funding acquisition.

DECLARATION OF INTERESTS

The authors declare no competing interests.

STAR★METHODS

Detailed methods are provided in the online version of this paper and include the following:

- KEY RESOURCES TABLE
- METHOD DETAILS

Received: May 9, 2024
Revised: September 20, 2024
Accepted: December 19, 2024
Published: December 21, 2024

REFERENCES

1. Elkholy, A.E., El-Taib Heakal, F., and Allam, N.K. (2019). A facile electrosynthesis approach of amorphous Mn-Co-Fe ternary hydroxides as binder-free active electrode materials for high-performance supercapacitors. Electrochim. Acta *296*, 59–68. https://doi.org/10.1016/j.electacta.2018.11.038.
2. Yu, F., Wei, P., Yang, Y., Chen, Y., Guo, L., and Peng, Z. (2019). Material design at nano and atomic scale for electrocatalytic CO2 reduction. Nano Mater. Sci. *1*, 60–69. https://doi.org/10.1016/j.nanoms.2019.03.006.
3. Zhao, Y., He, X., Chen, R., Liu, Q., Liu, J., Yu, J., Li, J., Zhang, H., Dong, H., Zhang, M., and Wang, J. (2018). A flexible all-solid-state asymmetric supercapacitors based on hierarchical carbon cloth@ CoMoO4@ NiCo layered double hydroxide core-shell heterostructures. Chem. Eng. J. *352*, 29–38. https://doi.org/10.1016/j.cej.2018.06.181.
4. Wang, G., Zhang, L., Yan, B., Luo, J., Su, X., and Yue, F. (2019). Oxygen vacancy-rich anatase TiO2 hollow spheres via liquid nitrogen quenching process for enhanced photocatalytic hydrogen evolution. ChemCatChem *11*, 1057–1063. https://doi.org/10.1002/cctc.201801721.
5. Li, K., Teng, H., Sun, Q., Li, Y., Wu, X., Dai, X., Wang, Y., Wang, S., Zhang, Y., Yao, K., et al. (2022). Engineering active sites on nitrogen-doped carbon nanotubes/cobaltosic oxide heterostructure embedded in biotemplate for high-performance supercapacitors. J. Energy Storage *53*, 105094. https://doi.org/10.1016/j.est.2022.105094.
6. Li, K., Yin, C., Dai, X., Zhang, J., Yi, S., Rao, J., and Zhang, Y. (2022). Facile synthesis and incomplete sulfidation of nickel-cobalt-aluminum ternary layered hydroxide binder-free electrode with enhanced supercapacitor properties. J. Energy Storage *55*, 105722. https://doi.org/10.1016/j.est.2022.105722.
7. Li, K., Xiao, Y., Zheng, T., Sun, Q., Zhang, Y., Teng, H., Wang, W., Yao, K., Rao, J., and Zhang, Y. (2023). Vanadium doping and phosphorus vacancy co-regulation of biotemplate derived three-dimensional cobalt phosphide to enhance pseudocapacitance performance. Appl. Surf. Sci. *622*, 156950. https://doi.org/10.1016/j.apsusc.2023.156950.

8. Jing, C., Huang, Y., Xia, L., Chen, Y., Wang, X., Liu, X., Dong, B., Dong, F., Li, S., and Zhang, Y. (2019). Growth of cobalt-aluminum layered double hydroxide nanosheets on graphene oxide towards high performance supercapacitors: The important role of layer structure. Appl. Surf. Sci. *496*, 143700. https://doi.org/10.1016/j.apsusc.2019.143700.

9. Divyashree, A., and Hegde, G. (2015). Activated carbon nanospheres derived from bio-waste materials for supercapacitor applications–a review. RSC Adv. *5*, 88339–88352. https://doi.org/10.1039/C5RA19392C.

10. Zhi, M., Xiang, C., Li, J., Li, M., and Wu, N. (2013). Nanostructured carbon–metal oxide composite electrodes for supercapacitors: a review. Nanoscale *5*, 72–88. https://doi.org/10.1039/C2NR32040A.

11. Sun, Q., Guo, Z., Shu, T., Li, Y., Li, K., Zhang, Y., Li, L., Ning, J., and Yao, K.X. (2024). Lithium-Induced Oxygen Vacancies in MnO2@MXene for High-Performance Zinc–Air Batteries. ACS Appl. Mater. Interfaces *16*, 12781–12792. https://doi.org/10.1021/acsami.3c18248.

12. Chandrasekaran, N.I., Muthukumar, H., Sekar, A.D., and Manickam, M. (2017). Hollow nickel-aluminium-manganese layered triple hydroxide nanospheres with tunable architecture for supercapacitor application. Mater. Chem. Phys. *195*, 247–258. https://doi.org/10.1016/j.matchemphys.2017.04.027.

13. Li, K., Guo, Z., Sun, Q., Dai, X., Li, Y., Yao, K., Liu, X., Bao, Z., Rao, J., and Zhang, Y. (2023). Phosphorus vacancy regulation and interfacial coupling of biotemplate derived CoP@FeP2 heterostructure to boost pseudocapacitive reaction kinetics. Chem. Eng. J. *454*, 140223. https://doi.org/10.1016/j.cej.2022.140223.

14. Helmholtz, H. (1853). Ueber einige Gesetze der Vertheilung elektrischer Ströme in körperlichen Leitern, mit Anwendung auf die thierisch-elektrischen Versuche (Schluss.). Ann. Phys. *165*, 353–377. https://doi.org/10.1002/andp.18531650702.

15. Wang, G., Zhang, L., and Zhang, J. (2012). A review of electrode materials for electrochemical supercapacitors. Chem. Soc. Rev. *41*, 797–828. https://doi.org/10.1039/C1CS15060J.

16. Choi, H., and Yoon, H. (2015). Nanostructured electrode materials for electrochemical capacitor applications. Nanomaterials *5*, 906–936. https://doi.org/10.3390/nano5020906.

17. Sevilla, M., and Mokaya, R. (2014). Energy storage applications of activated carbons: supercapacitors and hydrogen storage. Energy Environ. Sci. *7*, 1250–1280. https://doi.org/10.1039/C3EE43525C.

18. Xu, G., Han, J., Ding, B., Nie, P., Pan, J., Dou, H., Li, H., and Zhang, X. (2015). Biomass-derived porous carbon materials with sulfur and nitrogen dual-doping for energy storage. Green Chem. *17*, 1668–1674. https://doi.org/10.1039/C4GC02185A.

19. He, X., Liu, Q., Liu, J., Li, R., Zhang, H., Chen, R., and Wang, J. (2017). High-performance all-solid-state asymmetrical supercapacitors based on petal-like NiCo2S4/Polyaniline nanosheets. Chem. Eng. J. *325*, 134–143. https://doi.org/10.1016/j.cej.2017.05.043.

20. He, X., Li, R., Liu, J., Liu, Q., chen, R., Song, D., and Wang, J. (2018). Hierarchical FeCo2O4@ NiCo layered double hydroxide core/shell nanowires for high performance flexible all-solid-state asymmetric supercapacitors. Chem. Eng. J. *334*, 1573–1583. https://doi.org/10.1016/j.cej.2017.11.089.

21. Zhang, H., Usman Tahir, M., Yan, X., Liu, X., Su, X., and Zhang, L. (2019). Ni-Al layered double hydroxide with regulated interlayer spacing as electrode for aqueous asymmetric supercapacitor. Chem. Eng. J. *368*, 905–913. https://doi.org/10.1016/j.cej.2019.03.041.

22. Luo, F., San, X., Wang, Y., Meng, D., and Tao, K. (2024). Layered double hydroxide-based electrode materials derived from metal–organic frameworks: synthesis and applications in supercapacitors. Dalton Trans. *53*, 10403–10415. https://doi.org/10.1039/D4DT01344A.

23. kheradmand, A., Ghiasinejad, H., Javanshir, S., khadir, A., and jamshidi, E. (2021). Efficient removal of Ibuprofen via novel core – shell magnetic bio-surfactant rhamnolipid – layered double hydroxide nanocomposite. J. Environ. Chem. Eng. *9*, 106158. https://doi.org/10.1016/j.jece.2021.106158.

24. kheradmand, A., Negarestani, M., Kazemi, S., Shayesteh, H., Javanshir, S., Ghiasinejad, H., and Jamshidi, E. (2023). Design and preparation magnetic bio-surfactant rhamnolipid-layered double hydroxide nanocomposite as an efficient and recyclable adsorbent for the removal of Rifampin from aqueous solution. Sep. Purif. Technol. *304*, 122362. https://doi.org/10.1016/j.seppur.2022.122362.

25. Jamshidi, E., and Manteghi, F. (2020). Methyl orange adsorption by Fe2O3@ Co-Al-layered double hydroxide. Multidiscip. Digit. Publ. Inst. Proc. *41*, 64. https://doi.org/10.3390/ecsoc-23-06617.

26. Beigi, F., Mousavi, M.S.S., Manteghi, F., and Kolahdouz, M. (2018). Doped nafion-layered double hydroxide nanoparticles as a modified ionic polymer metal composite sheet for a high-responsive humidity sensor. Appl. Clay Sci. *166*, 131–136. https://doi.org/10.1016/j.clay.2018.09.006.

27. Xu, Y. (2017). Hierarchical materials. In Modern inorganic synthetic chemistry (Elsevier), pp. 545–574. https://doi.org/10.1016/B978-0-444-63591-4.00019-7.

28. Daniel, S., and Thomas, S. (2020). Layered double hydroxides: fundamentals to applications. In Layered double hydroxide polymer nanocomposites (Elsevier), pp. 1–76. https://doi.org/10.1016/B978-0-323-91894-7.00016-5.

29. Li, T., Hu, X., Yang, C., Han, L., and Tao, K. (2023). A heterostructure of NiMn-LDH nanosheets assembled on ZIF-L-derived ZnCoS hollow nanosheets with a built-in electric field enables boosted electrochemical energy storage. Dalton Trans. *52*, 16640–16649. https://doi.org/10.1039/D3DT02931J.

30. Yang, W., Gao, Z., Wang, J., Ma, J., Zhang, M., and Liu, L. (2013). Solvothermal one-step synthesis of Ni–Al layered double hydroxide/carbon nanotube/reduced graphene oxide sheet ternary nanocomposite with ultrahigh capacitance for supercapacitors. ACS Appl. Mater. Interfaces *5*, 5443–5454. https://doi.org/10.1021/am4003843.

31. Miller, E.E., Hua, Y., and Tezel, F.H. (2018). Materials for energy storage: Review of electrode materials and methods of increasing capacitance for supercapacitors. J. Energy Storage *20*, 30–40. https://doi.org/10.1016/j.est.2018.08.009.

32. Huang, Q., Liu, K., Fang, H.E., Zhang, S., Xie, Q., and Cheng, C. (2017). Fabrication of cobalt aluminum-layered double hydroxide nanosheets/carbon spheres composite as novel electrode material for supercapacitors. Trans. Nonferrous Metals Soc. China *27*, 1804–1814. https://doi.org/10.1016/S1003-6326(17)60203-6.

33. Hao, Q., Xia, X., Lei, W., Wang, W., and Qiu, J. (2015). Facile synthesis of sandwich-like polyaniline/boron-doped graphene nano hybrid for supercapacitors. Carbon N. Y. *81*, 552–563. https://doi.org/10.1016/j.carbon.2014.09.090.

34. Bi, Q., Hu, X., and Tao, K. (2023). MOF-derived NiCo-LDH Nanocages on CuO Nanorod Arrays for Robust and High Energy Density Asymmetric Supercapacitors. Chem. Eur J. *29*, e202203264. https://doi.org/10.1002/chem.202203264.

35. Mondal, S., Rana, U., and Malik, S. (2015). Graphene quantum dot-doped polyaniline nanofiber as high performance supercapacitor electrode materials. Chem. Commun. *51*, 12365–12368. https://doi.org/10.1039/C5CC03981A.

36. Yang, Y., Ren, S., Song, X., Guo, Y., Si, D., Jing, H., Ma, S., Hao, C., and Ji, M. (2016). Sn@ SnO2 attached on carbon spheres as additive-free electrode for high-performance pseudocapacitor. Electrochim. Acta *209*, 350–359. https://doi.org/10.1016/j.electacta.2016.05.105.

37. Tao, Y., Ruiyi, L., Tingting, Y., and Zaijun, L. (2015). Nickel/cobalt layered double hydroxide hollow microspheres with hydrangea-like morphology for high-performance supercapacitors. Electrochim. Acta *152*, 530–537. https://doi.org/10.1016/j.electacta.2014.08.149.

38. Yan, T., Li, R., and Li, Z. (2014). Nickel–cobalt layered double hydroxide ultrathin nanoflakes decorated on graphene sheets with a 3D nanonetwork structure as supercapacitive materials. Mater. Res. Bull. *51*, 97–104. https://doi.org/10.1016/j.materresbull.2013.11.044.

39. Nakamoto, K. (1997). Infrared and Raman Spectra of Inorganic and Coordination Compounds (Part A: Theory and Applications in Inorganic Chemistry)(Volume 1A)(Part B: Applications in Coordination, Organometallic, and Bioinorganic Chemistry)(Volume 1B) (John Wiley & Sons, Incorporated).

40. Bathla, A., and Pal, B. (2018). Catalytic selective hydrogenation and cross coupling reaction using polyvinylpyrrolidone-capped nickel nanoparticles. ChemistrySelect *3*, 4738–4744. https://doi.org/10.1002/slct.201800699.

41. Lei, X., Zhang, F., Yang, L., Guo, X., Tian, Y., Fu, S., Li, F., Evans, D.G., and Duan, X. (2007). Highly crystalline activated layered double hydroxides as solid acid-base catalysts. AIChE J. *53*, 932–940. https://doi.org/10.1002/aic.11118.

42. Sj, G., and Sing, K.S.W. (1982). Adsorption, surface area and porosity. J. Electrochem. Soc. *114*, 279Ca, Acad. Press. New York. https://doi.org/10.1149/1.2426447.

43. Botan, R., Nogueira, T.R., Wypych, F., and Lona, L.M.F. (2012). In situ synthesis, morphology, and thermal properties of polystyrene—MgAl layered double hydroxide nanocomposites. Polym. Eng. Sci. *52*, 1754–1760. https://doi.org/10.1002/PEN.23122.

44. Liu, B., Dai, Y.-K., Li, L., Zhang, H.-D., Zhao, L., Kong, F.-R., Sui, X.-L., and Wang, Z.-B. (2020). Effect of polytetrafluoroethylene (PTFE) in current collecting layer on the performance of zinc-air battery. Prog. Nat. Sci. Mater. Int. *30*, 861–867. https://doi.org/10.1016/j.pnsc.2020.09.012.

45. Yadav, S., Ghrera, A.S., and Devi, A. (2023). Hierarchical grass-like NiCo2O4 nanowires grown on nickel foam as a binder-free supercapacitor electrode. Mater. Today Proc. *74*, 281–288. https://doi.org/10.1016/j.matpr.2022.08.240.

46. Wang, X., Li, H., Li, H., Lin, S., Bai, J., Dai, J., Liang, C., Zhu, X., Sun, Y., and Dou, S. (2019). Heterostructures of Ni–Co–Al layered double hydroxide assembled on V 4 C 3 MXene for high-energy hybrid supercapacitors. J. Mater. Chem. A *7*, 2291–2300. https://doi.org/10.1039/C8TA11249E.

47. Li, J., Zhang, P., Zhao, X., Chen, L., Shen, J., Li, M., Ji, B., Song, L., Wu, Y., and Liu, D. (2019). Structure-controlled Co-Al layered double hydroxides/reduced graphene oxide nanomaterials based on solid-phase exfoliation technique for supercapacitors. J. Colloid Interface Sci. *549*, 236–245. https://doi.org/10.1016/j.nanoen.2016.08.049.

48. Zhang, Q., Zhao, B., Wang, J., Qu, C., Sun, H., Zhang, K., and Liu, M. (2016). High-performance hybrid supercapacitors based on self-supported 3D ultrathin porous quaternary Zn-Ni-Al-Co oxide nanosheets. Nano Energy *28*, 475–485. https://doi.org/10.1016/j.electacta.2016.12.160.

49. Wang, X., Lin, Y., Su, Y., Zhang, B., Li, C., Wang, H., and Wang, L. (2017). Design and synthesis of ternary-component layered double hydroxides for high-performance supercapacitors: understanding the role of trivalent metal ions. Electrochim. Acta *225*, 263–271. https://doi.org/10.1016/j.electacta.2016.12.160.

50. Ma, X., Wang, S., Wang, H., Ding, J., Liu, S., Huang, Z., Sun, W., Liu, G., Wang, L., and Xu, W. (2022). Construction of high-performance asymmetric supercapacitor based on FeCo-LDH@ C3N4 composite electrode material with penetrating structure. J. Energy Storage *56*, 106034. https://doi.org/10.1016/j.est.2022.106034.

51. Hu, H., Cai, B., Jiang, Y., Li, X., Wang, J., Wang, L., Yang, X., and Lü, W. (2023). Ni3S2@ NiCo-LDH cross-linked nanosheet arrays on Ni foam for high-performance all-solid-state asymmetric supercapacitors. J. Alloys Compd. *953*, 169869. https://doi.org/10.1016/j.jallcom.2023.169869.

52. Zhai, D., Wen, J., Ding, Q., Feng, Y., and Yang, W. (2023). Hierarchical design of NiCo-LDH NFs@ Co (OH) 2 nanosheets supercapacitor electrode material with boosted electrochemical performance. Int. J. Hydrogen Energy *48*, 10108–10117. https://doi.org/10.1016/j.ijhydene.2022.12.128.

53. Xiong, H., Liu, L., Fang, L., Wu, F., Zhang, S., Luo, H., Tong, C., Hu, B., and Zhou, M. (2021). 3D self-supporting heterostructure NiCo-LDH/ZnO/CC electrode for flexible high-performance supercapacitor. J. Alloys Compd. *857*, 158275. https://doi.org/10.1016/j.jallcom.2020.158275.

54. Wang, J., Ding, Q., Bai, C., Wang, F., Sun, S., Xu, Y., and Li, H. (2021). Synthesis of CNTs/CoNiFe-LDH nanocomposite with high specific surface area for asymmetric supercapacitor. Nanomaterials *11*, 2155. https://doi.org/10.3390/nano11092155.

55. Dinari, M., Allami, H., and Momeni, M.M. (2020). Construction of Ce-doped NiCo-LDH@ CNT nanocomposite electrodes for high-performance supercapacitor application. Energy Fuels *35*, 1831–1841. https://doi.org/10.1021/acs.energyfuels.0c03764.

56. Chen, F., Chen, C., Hu, Q., Xiang, B., Song, T., Zou, X., Li, W., Xiong, B., and Deng, M. (2020). Synthesis of CuO@ CoNi LDH on Cu foam for high-performance supercapacitors. Chem. Eng. J. *401*, 126145. https://doi.org/10.1016/j.cej.2020.126145.

57. Su, L.-H., Zhang, X.-G., and Liu, Y. (2008). Electrochemical performance of Co–Al layered double hydroxide nanosheets mixed with multiwall carbon nanotubes. J. Solid State Electrochem. *12*, 1129–1134. https://doi.org/10.1016/S1003-6326(17)60203-6.

58. Han, J., Dou, Y., Zhao, J., Wei, M., Evans, D.G., and Duan, X. (2013). Flexible CoAl LDH@ PEDOT core/shell nanoplatelet array for high-performance energy storage. Small *9*, 98–106. https://doi.org/10.1002/smll.201201336.

59. Cheng, J.P., Fang, J.H., Li, M., Zhang, W.F., Liu, F., and Zhang, X.B. (2013). Enhanced electrochemical performance of CoAl-layered double hydroxide nanosheet arrays coated by platinum films. Electrochim. Acta *114*, 68–75. https://doi.org/10.1016/j.electacta.2013.10.029.

60. Sawangphruk, M., Suksomboon, M., Kongsupornsak, K., Khuntilo, J., Srimuk, P., Sanguansak, Y., Klunbud, P., Suktha, P., and Chiochan, P. (2013). High-performance supercapacitors based on silver nanoparticle–polyaniline–graphene nanocomposites coated on flexible carbon fiber paper. J. Mater. Chem. A *1*, 9630–9636. https://doi.org/10.1039/C3TA12194A.

61. Sinan, N., and Unur, E. (2016). Fe3O4/carbon nanocomposite: Investigation of capacitive & magnetic properties for supercapacitor applications. Mater. Chem. Phys. *183*, 571–579. https://doi.org/10.1016/j.matchemphys.2016.09.016.

62. Salanne, M., Rotenberg, B., Naoi, K., Kaneko, K., Taberna, P.-L., Grey, C.P., Dunn, B., and Simon, P. (2016). Efficient storage mechanisms for building better supercapacitors. Nat. Energy *1*, 16070–16110. https://doi.org/10.1038/nenergy.2016.70.

63. Jaji, N.-D., Othman, M.B.H., Lee, H.L., Hussin, M.H., and Hui, D. (2021). One-pot solvothermal synthesis and characterization of highly stable nickel nanoparticles. Nanotechnol. Rev. *10*, 318–329. https://doi.org/10.1515/ntrev-2021-0019.

STAR★METHODS

KEY RESOURCES TABLE

REAGENT or RESOURCE	SOURCE	IDENTIFIER
Cobalt (II) nitrate hexahydrate	Sigma Aldrich	10026-22-9
Aluminum nitrate nonahydrate	Sigma Aldrich	7784-27-2
Nickel (II) chloride hexahydrate	Sigma Aldrich	7791-20-0
Sodium carbonate	Sigma Aldrich	497-19-8
Sodium acetate	Sigma Aldrich	127-09-3
Ethylene glycol	Sigma Aldrich	107-21-1
Ammonia solution	Sigma Aldrich	1336-21-6

METHOD DETAILS

The chemical reagents utilized in this experiment were all purchased from Aldrich and were not purified further. To prepare the CoAl-LDH, the $Co(NO_3)_2 \cdot 6H_2O$ and $Al(NO_3)_3 \cdot 9H_2O$ (molar ratio 3:1) were dissolved in 30 mL of deionized water under ultrasound irradiation until the final concentration of the metal cations reaches to 0.5 mol L^{-1} leading to a monodispersed solution of both metal salts. Then 0.1 M solution of Na_2CO_3 was added dropwisely to the as-prepared solution containing metal salts, to raise the pH up to 10. After 2h of stirring at 55°*C*, the stirring process stopped and the temperature raised to 70°*C*. The final solution was rested at 70°*C* for 24h, after filtration and washing with deionized water, the pink powder was dried in a vacuum oven at 65°*C* for 10h.

Microspheres of Ni were prepared by the solvothermal method reported previously. Primarily, 3.2 g of $NiCl_2 \cdot 6H_2O$ and 8.6 g of $CH_3COONa \cdot 3H_2O$ were dissolved in 85 mL ethylene glycol, then the ultrasound irradiation was applied at 70°C during 20 min followed by stirring for 30 min until a deep blue homogeneous solution was formed. The solution was transferred into an autoclave with an interior coating of PTFE and heated at 240°C for 8 h. After cooling the provided suspension, it was filtered followed by washing with deionized water and ethanol alternatively three times. The final precipitate was dried in a vacuum oven to obtain the Ni powder.[63]

The title core-shell nanocomposite of nickel and LDH was synthesized with the co-precipitation method (Scheme 4). To embed CoAl-LDH nanosheets on the as-prepared Ni nanoparticles, $Co(NO_3)_2 \cdot 6H_2O$ and $Al(NO_3)_3 \cdot 9H_2O$ (molar ratio 3:1) were dissolved in 30 mL of deionized water under ultrasound irradiation until final concentration of the metal cations reaches to 0.5 mol L^{-1} leading to a monodispersed solution of both metal salts.

Afterward, the as-prepared Ni powder was added to the metal salts' solution under ultrasound irradiation. To form the LDH nanosheets, the media was made alkaline using the aqueous solution of ammonia (with a volume ratio of 1:4) dropwise at 50°C until the suspension pH reached to 10. In this stage, the precipitation of CoAl-LDH as a violet layer around the Ni core was observed. After resting the solution at room temperature for 1 h, To get the dry powder of Ni@CoAl-LDH, the prepared suspension was filtered, washed four times with deionized water, and dried in a vacuum oven at 80°C.